

ARSAR-Net: Intelligent SAR Imaging with Adaptive Regularization

Shiping Fu, Yufan Chen, Zhe Zhang, Xiaolan Qiu, Qixiang Ye

Abstract—Deep unfolding networks have recently emerged as a promising approach for synthetic aperture radar (SAR) imaging. However, baseline unfolding networks, typically derived from iterative reconstruction algorithms such as the alternating direction method of multipliers (ADMM), lack generalization capability across scenes, primarily because their regularizers are empirically designed rather than learned from data. In this study, we introduce a learnable regularizer into the unfolding network and propose a SAR imaging network with adaptive regularization (ARSAR-Net), which aims to generalize across heterogeneous scenes including offshore ships, islands, urban areas, and mountainous terrain. Furthermore, two variants of ARSAR-Net are developed, targeting improved imaging efficiency and reconstruction quality, respectively. Extensive validation through simulated and real-data experiments demonstrates three key advantages of ARSAR-Net: (1) a 50% increase in imaging speed over existing unfolding networks, (2) a PSNR gain of up to 2.0 dB in imaging quality, and (3) enhanced adaptability to complex scenes. These advancements establish a new paradigm for computationally efficient and generalizable SAR imaging systems.

Index Terms—Synthetic aperture radar imaging, Sparse microwave imaging, Adaptive regularization, Deep unfolding network.

I. INTRODUCTION

Synthetic aperture radar (SAR), as an important microwave imaging technique, has been widely utilized in diverse applications including remote sensing, earth observation, mapping, forestry, agriculture, and military reconnaissance [1]–[4], due to its unique all-weather/all-time operational reliability and high-resolution imaging capacity [5], [6]. Conventional widely-used SAR imaging techniques, such as the range-Doppler algorithm (RDA) [7] and the chirp scaling algorithm (CSA) [8], typically use matched filtering (MF) techniques. In recent decades, sparse signal processing, represented by compressed sensing (CS) theory, has been introduced into SAR imaging. Sparse SAR imaging not only enables successful imaging from fewer measurements than those traditionally required by the Nyquist theory but also improves SAR imaging performance, such as achieving lower sidelobes and better ambiguity suppression [9]. Although sparse SAR imaging has been widely adopted for sparse scenes, the generalization capability of these methods remains insufficient, as the hand-crafted regularizers, often based on the ℓ_1 -norm, lack adaptability when processing echo signals from scenes of various sparsity degrees or different scene types.

Most recently, unfolding networks [10] have emerged as a promising method for SAR imaging. As shown in Fig. 1, these networks are constructed by unfolding iterative reconstruction

algorithms such as the iterative shrinkage-thresholding algorithm (ISTA) [11] and the alternating direction method of multiplier (ADMM) [12] into a neural network with learnable parameters.

To address the computational complexity issue, approximated observation operators constructed from MF algorithms [13] have also been adopted. In this way, these approaches take advantage of both model-driven algorithms and data-driven networks, achieving enhanced performance while enjoying interpretability. However, the baseline unfolding networks remain challenged by scene generalization capability as the regularizers are simple and empirically chosen, lacking the ability to adaptively learn from data. The design of unfolding networks equipped with more expressive and learnable regularizers remains to be explored.

A. Related work

Compressed sensing-inspired regularization approaches [14] have shown great potential when reconstructing sparse signals from limited observation data. As a classical regularizer, ℓ_1 -norm minimization [15] is commonly formulated as a regularized inverse optimization problem, reconstructing target scenes by solving an objective function [16]. Considering the scattered field of SAR is sparse, iterative algorithms such as orthogonal matching pursuit (OMP) [17], compressive sampling matching pursuit (CoSaMP) [18], iterative shrinkage-thresholding algorithm (ISTA), and fast iterative shrinkage-thresholding algorithm (FISTA) [19] can be applied. However, despite their effectiveness in sparse scenes, these methods struggle to define a general sparse basis for scenes of different sparsity degrees.

To address the adaptive sparsity issue, structural sparse representation [20], [21] is proposed to formulate SAR image reconstruction and sparse space updating as a joint optimization problem. In addition, combined dictionaries with structured sparsity [22] are also proposed for adaptive sensing. While these improvements enable direct processing of downsampled raw data, they remain challenged by space-borne SAR imaging when handling large-scale measurement matrices.

To conquer the challenge of large-scale matrices, approximated observation operators based on matched filters [13] are proposed to reconstruct sparse scenes from downsampling data for high-quality imaging with efficiency. An efficient ℓ_q regularization algorithm [23], constructed using a decoupling operator based on the chirp scaling algorithm, reduces the computational complexity from quadratic to linear order. While these methods address data storage and processing problems, they face two major challenges. First, compressed sensing methods typically involve numerous hyperparameters that need to be manually tuned. Secondly, conventional sparse

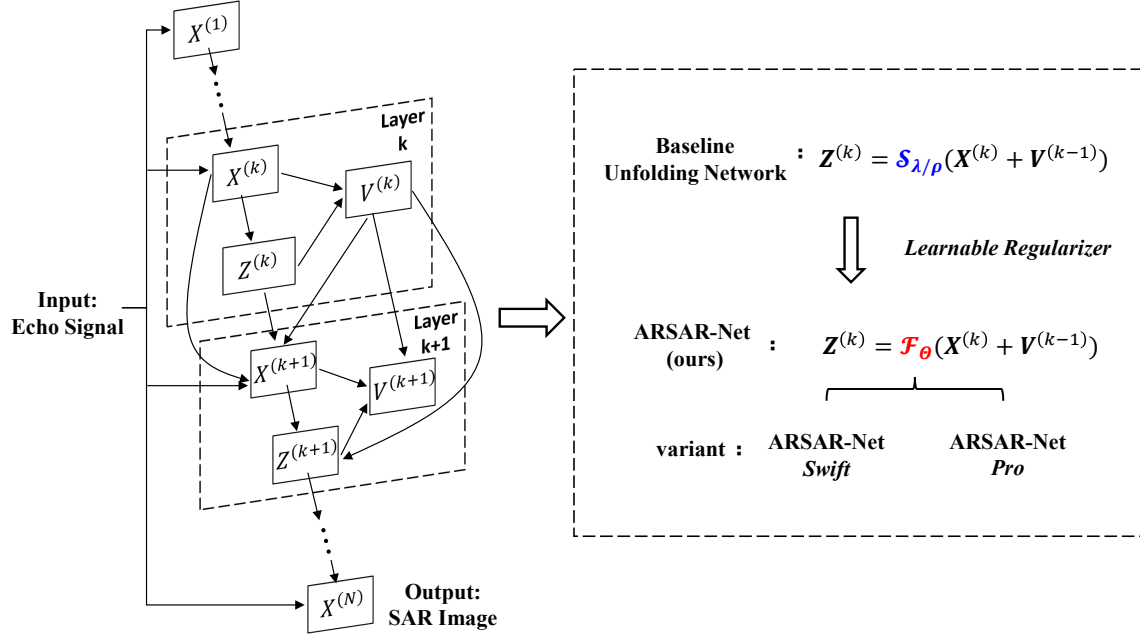


Fig. 1. SAR imaging with unfolding networks. The baseline unfolding network is enhanced to ARSAR-Net (with two variants) by introducing a learnable regularizer.

representation methods require both a specific sparse basis and a predefined regularization tailored to the target SAR scattering field. Consequently, their adaptability is constrained by the need for manual hyperparameter tuning and the reliance on specific prior modeling.

As a data-driven approach, deep learning (DL) methods can learn representations from the training data, avoiding hand-crafted modeling and parameter tuning. In the signal and image processing field, deep neural networks (DNNs) demonstrate remarkable effectiveness, offering innovative solutions for SAR imaging [24], [25]. A complex-valued convolutional neural network (CV-CNN) [26] is employed to explore the potential of applying deep neural networks (DNNs) to radar imaging. Moreover, DeepImaging [27], a CNN-based method, is applied to multiple target imaging, achieving significant improvements in both imaging quality and efficiency.

In contrast to CNNs, unfolding networks leverage the interpretability of iterative algorithms and the generalization capacity of deep learning [28]. DUNs transform each iteration of conventional compressed sensing-driven iterative algorithms into a corresponding layer of a deep network, resulting in unfolding networks. Specifically, each iteration of iterative algorithms is transformed into a trainable neural network layer, forming the unfolding networks. Such networks achieved enhanced imaging performance and interpretability and have been widely investigated. For instance, a representative unfolding network, AF-AMPNet [29], employs an unfolding architecture for inverse synthetic aperture radar (ISAR) imaging. LFIST-Net [30] constructs a lightweight holographic network based on FISTA, achieving higher flexibility for 3D millimeter-wave imaging.

Motivated by these studies, deep unfolding methods for SAR imaging have gained significant attention [31]–[34]. To

enhance the signal-to-clutter ratio (SCR) of reconstructed images, a target-oriented SAR imaging model incorporating generalized regularization is proposed [35]. Building upon ADMM optimization, LRSR-ADMM-Net [36] formulates SAR imaging as a joint low-rank and sparse matrix recovery problem, while TADMM-Net [37] extends this framework with improvements that boost its ability to handle two-dimensional signals. For non-sparse scenes, SR-ISTA-Net [38] and SR-CSA-Net [39], designed as ISTA-based unfolding networks that employ CSA-generated imaging operators, leverage neural networks to model the imaging process. Additionally, NSR-Net [40] utilizes a neural network to learn a representation by approximating the iterative solution obtained via proximal gradient descent (PGD). Nevertheless, despite improved learning capabilities, computational efficiency remains a significant challenge.

In recent years, learnable regularization has emerged as a groundbreaking approach. This type of regularization can be implemented via denoisers or neural networks, serving as a data-driven alternative to conventional regularizers in iterative reconstruction frameworks such as ADMM. This paradigm has found applications across a wide range of domains. A representative example is the plug-and-play prior framework [41], which replaces the traditional regularizer with a denoiser for magnetic resonance imaging (MRI) reconstruction. Furthermore, ADMM-CSNet [42] embeds a CNN-based optimization module with nonlinear piecewise functions into the ADMM framework, achieving superior performance and efficiency in MRI and optical image reconstruction. Inspired by these advances, ARSAR-Net is developed in this study to further explore the potential of learnable regularization in SAR imaging.

B. Contributions

In this paper, we propose a SAR imaging network with adaptive regularization (ARSAR-Net) to enhance generalization capability across scenes with varying sparsity degrees.¹ ARSAR-Net is built upon an unfolding network that follows the framework of ADMM without matrix inversion. To overcome the limitations of empirically designed regularizers, ARSAR-Net introduces a learnable regularizer, enabling the model to adapt to diverse scene characteristics. In Fig. 1, we show the framework of ARSAR-Net and its improvements over the baseline unfolding network. The contributions of this study are summarized as follows.

- A SAR imaging model tailored for 2D echo signal processing is first constructed using the ADMM algorithm without matrix inversion. Building upon this model, we develop ARSAR-Net, which incorporates a learnable regularizer to improve the generalization capability across scenes.
- To meet the varying demands of SAR imaging applications, two variants of ARSAR-Net are proposed: ARSAR-Net Swift, optimized for high-speed imaging, and ARSAR-Net Pro, designed for high-fidelity reconstruction.
- Extensive experiments demonstrate the superiority of ARSAR-Net over existing methods. When handling real echo signals, ARSAR-Net achieves up to 50% faster imaging speed than recent unfolding networks, while also improving imaging PSNR by up to 2 dB.

The remainder of this paper is organized as follows. Section II discusses the 2D SAR imaging model based on the ADMM algorithm without matrix inversion. Section III provides a detailed description of ARSAR-Net and its variants. Section IV presents experimental results and performance analysis. Finally, Section V concludes the paper.

II. 2D SAR IMAGING MODEL

To make the section self-contained, we first introduce a 2D SAR imaging model based on CSA operators within the conventional ADMM framework. However, the direct integration of ADMM with 2D SAR imaging suffers from structural limitations, hindering practical implementation. To overcome this challenge, we adopt an ADMM algorithm without matrix inversion and formulate an enhanced imaging model suitable for 2D echo signal processing.

A. 2D Imaging Model and Problems

In this study, the vertical side-looking strip mode is employed in the SAR system as shown in Fig. 2.

The SAR imaging model establishes a mathematical relationship between the radar echo signal and the scattering coefficients of the observed area. For numerical processing, the observation area is discretized to a grid of $M \times N$ scattering centers, where the indices $m = 1, 2, \dots, M$ and $n = 1, 2, \dots, N$ denote discrete positions along the range and azimuth directions, respectively. This discretization allows

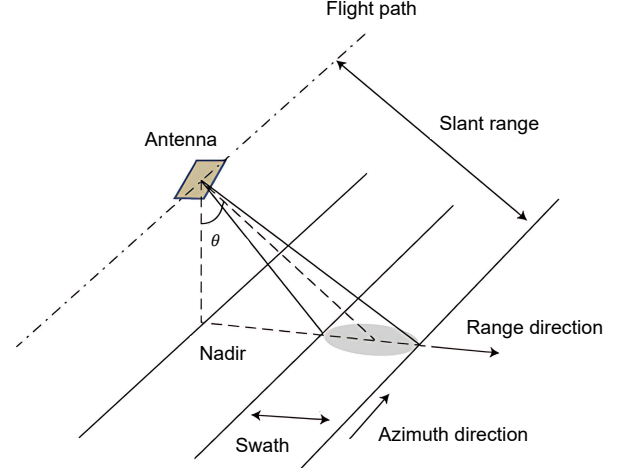


Fig. 2. Geometric Structure of SAR Imaging System (Credit: NASA). [43]

the scattering coefficients to be denoted as a 2D matrix $\mathbf{X} \in \mathbb{C}^{M \times N}$. Similarly, the echo signal is represented as $\mathbf{Y} \in \mathbb{C}^{M \times N}$.

To characterize the relationship between them, the echo signal is modeled by the observation matrix $\Phi \in \mathbb{C}^{MN \times MN}$ which acts on the vectorized scattering coefficient $\mathbf{x} = \text{vec}(\mathbf{X})$ to produce the vectorized echo signal $\mathbf{y} = \text{vec}(\mathbf{Y})$, i.e.,

$$\mathbf{y} = \Phi \mathbf{x} \quad (1)$$

where $\text{vec}(\cdot)$ denotes the vectorization operator stacking the matrix columns into a single vector. To simulate reduced observations, the echo signal is further downsampled by applying $\Psi_r \in \mathbb{R}^{M' \times M}$ (range) and $\Psi_a \in \mathbb{R}^{N' \times N}$ (azimuth), yielding the downsampled echo $\mathbf{Y}_d \in \mathbb{C}^{M' \times N'}$.

It can be seen that vectorization leads to a large observation matrix size. For example, converting an $N \times N$ echo signal into a vector results in a $N^2 \times N^2$ observation matrix Φ , substantially increasing storage requirements and computational costs. Moreover, the inherent azimuth-range coupling further complicates the direct decoupling of the observation matrix.

To address these issues, the matched filter technique approximates Φ using a series of 1D operators along the azimuth and range directions [13]. These operators are efficiently implemented via the chirp scaling algorithm (CSA) [44], which directly constructs the imaging operator $\mathcal{M}(\cdot)$ and its approximate inverse, the observation operator $\mathcal{H}(\cdot)$, as

$$\begin{aligned} \mathcal{M}(\mathbf{Y}) &= \langle \mathbf{F}_r^H \{ \mathbf{F}_r [(\mathbf{Y} \mathbf{F}_a) \circ \Theta_s] \circ \Theta_r \} \circ \Theta_a \rangle \mathbf{F}_a^H, \\ \mathcal{H}(\mathbf{X}) &= \langle \mathbf{F}_r^H \{ \mathbf{F}_r [(\mathbf{X} \mathbf{F}_a) \circ \Theta_a^*] \circ \Theta_r^* \} \circ \Theta_s^* \rangle \mathbf{F}_a^H, \end{aligned} \quad (2)$$

where \circ denotes the Hadamard product. \mathbf{F}_r and \mathbf{F}_a are the FFT matrices along the range and azimuth directions, respectively. \mathbf{F}_r^H and \mathbf{F}_a^H denote the IFFT matrices. Θ_s , Θ_r , and Θ_a are the quadratic phase function for chirp scaling operation, the phase function for range compression and bulk range cell migration correction (RCMC), and the phase function for azimuth compression and residual phase compensation, respectively.

By leveraging the CSA-based operators, the large observation matrix Φ can be effectively replaced, enabling the

¹Code is available at <https://github.com/ShipenFyu/ARSAR-Net>.

reconstruction of the scattering coefficient \mathbf{X} from the measured echo signal \mathbf{Y} . To solve this inverse problem, we adopt the alternating direction method of multipliers (ADMM), a robust optimization algorithm widely used in regularized reconstruction. By introducing dual variables, ADMM decomposes the problem into separable subproblems, allowing flexible handling of various regularization terms. Furthermore, ADMM incorporates a quadratic penalty term in the augmented Lagrangian, which enhances convergence [45].

Through ADMM, the reconstruction problem is decomposed into two separable parts involving \mathbf{X} and auxiliary variable \mathbf{Z} , as

$$\begin{aligned} \min_{\mathbf{X}} \quad & \|\mathcal{G}(\mathbf{X}) - \mathbf{Y}_d\|_2^2 + \lambda\phi(\mathbf{Z}) \\ \text{s.t.} \quad & \mathbf{Z} = \mathbf{X}, \end{aligned} \quad (3)$$

where $\mathcal{G}(\cdot) = \Psi_r \mathcal{H}(\cdot) \Psi_a$ denotes the observation operator incorporating the downsampling matrices Ψ_r and Ψ_a , λ is the regularization factor, and $\phi(\cdot)$ represents an arbitrary regularization function such as ℓ_1 norm or TV regularization.

Accordingly, an augmented Lagrangian function is constructed, where the variable \mathbf{U} is the dual variable and ρ is the penalty parameter, as

$$\begin{aligned} L_\rho(\mathbf{X}, \mathbf{Z}, \mathbf{U}) = & \|\mathbf{Y}_d - \mathcal{G}(\mathbf{X})\|_2^2 + \lambda\phi(\mathbf{Z}) \\ & + \frac{\rho}{2} \|\mathbf{Z} - \mathbf{X}\|_2^2 + \langle \mathbf{U}, \mathbf{Z} - \mathbf{X} \rangle. \end{aligned} \quad (4)$$

From Eq. 4, the k -th iteration of ADMM is derived by decomposing the problem into three sequential updates, as follows:

$$\begin{cases} \mathbf{X}^{(k)} = \arg \min_{\mathbf{X}} \|\mathbf{Y}_d - \mathcal{G}(\mathbf{X})\|_2^2 \\ \quad + \frac{\rho}{2} \|\mathbf{X} - \mathbf{Z}^{(k-1)} + \mathbf{V}^{(k-1)}\|_2^2 & (5a) \\ \mathbf{Z}^{(k)} = \arg \min_{\mathbf{Z}} \lambda\phi(\mathbf{Z}) \\ \quad + \frac{\rho}{2} \|\mathbf{X}^{(k)} - \mathbf{Z} + \mathbf{V}^{(k-1)}\|_2^2 & (5b) \\ \mathbf{V}^{(k)} = \mathbf{V}^{(k-1)} + \mathbf{X}^{(k)} - \mathbf{Z}^{(k)} & (5c) \end{cases}$$

where $\mathbf{V} = 1/\rho \cdot \mathbf{U}$ is the scaled dual variable.

Suppose that $\mathcal{G}(\cdot)$ in Subproblem 5a is represented as a single matrix $\mathbf{\Gamma}$, the subproblem admits an explicit iterative solution:

$$\mathbf{X}^{(k)} = [\mathbf{\Gamma}^H \mathbf{\Gamma} + \rho \mathbf{I}]^{-1} [\mathbf{\Gamma}^H \mathbf{Y}_d + \rho(\mathbf{Z}^{(k-1)} - \mathbf{V}^{(k-1)})], \quad (8)$$

where \mathbf{I} denotes the identity matrix.

However, the observation operator $\mathcal{G}(\cdot)$, formulated in Eq. 6, combines matrix multiplications and Hadamard products, resulting in a complex mathematical structure. Therefore, the 2D imaging model cannot derive an explicit iterative solution of

scattering coefficient \mathbf{X} via matrix inversion. Consequently, the conventional ADMM is ill-suited for 2D SAR imaging.

B. Imaging Model based on ADMM without matrix inversion

To resolve the incompatibility between conventional ADMM and 2D SAR imaging, we adopt the ADMM algorithm without matrix inversion. Based on this, we develop an enhanced 2D SAR imaging model. The solution methods for Subproblem \mathbf{X} in Eq. 5a and Subproblem \mathbf{Z} in Eq. 5b are derived as follows.

1) *Subproblem X*: Several alternatives [37], [46] to the conventional ADMM have been proposed to eliminate matrix inversion. In this section, we employ a strategy that replaces matrix inversion with a Taylor expansion-based linear approximation to solve the subproblem \mathbf{X} under 2D echo signal conditions.

Let $S(\mathbf{X})$ denote the objective function to be optimized in the subproblem \mathbf{X} in Eq. 5a, which is formulated as

$$\begin{aligned} S(\mathbf{X}^{(k)}) = & \|\mathcal{G}(\mathbf{X}^{(k)}) - \mathbf{Y}_d\|_2^2 \\ & + \frac{\rho}{2} \|\mathbf{X}^{(k)} - \mathbf{Z}^{(k-1)} + \mathbf{V}^{(k-1)}\|_2^2. \end{aligned} \quad (9)$$

We carry out a second-order Taylor expansion of the objective function $S(\mathbf{X})$ while truncating higher-order terms.

$$\begin{aligned} \mathbf{X}^{(k)} = & \arg \min_{\mathbf{X}} S(\mathbf{X}) \\ \approx & \arg \min_{\mathbf{X}} S(\mathbf{X}^{(k-1)}) + \nabla S(\mathbf{X}^{(k-1)})^H (\mathbf{X} - \mathbf{X}^{(k-1)}) \\ & + \frac{1}{2} (\mathbf{X} - \mathbf{X}^{(k-1)})^H \nabla^2 S(\mathbf{X}^{(k-1)}) (\mathbf{X} - \mathbf{X}^{(k-1)}), \end{aligned}$$

where the second-order gradient matrix $\nabla^2 S(\mathbf{X}^{(k-1)})$ refers to the Hessian matrix [47].

Since the observation operator $\mathcal{G}(\cdot)$ in $S(\mathbf{X})$ is approximately linear under practical radar system configurations, the Hessian matrix can be reasonably approximated as constant, which is thoroughly explained in Appendix A, and expressed as

$$\begin{aligned} \mathbf{X}^{(k)} \approx & \arg \min_{\mathbf{X}} S(\mathbf{X}^{(k-1)}) + \nabla S(\mathbf{X}^{(k-1)})^H (\mathbf{X} - \mathbf{X}^{(k-1)}) \\ & + \frac{L}{2} \|\mathbf{X} - \mathbf{X}^{(k-1)}\|_2^2, \end{aligned} \quad (10)$$

where L denotes the Lipschitz constant, thus simplifying the iteration.

Through derivation of the optimization problem Eq. 10, we have the closed-form solution², as

$$\begin{aligned} \mathbf{X}^{(k)} = & (1 - \rho_n) \mathbf{X}^{(k-1)} + \mu \mathcal{T} [\mathbf{Y}_d - \mathcal{G}(\mathbf{X}^{(k-1)})] \\ & + \rho_n (\mathbf{Z}^{(k-1)} - \mathbf{V}^{(k-1)}), \end{aligned} \quad (11)$$

²Please refer to Appendix B for the detailed derivation.

$$\mathcal{G}(\mathbf{X}) = \Psi_r \langle \mathbf{F}_r^H \{ \mathbf{F}_r [(X \mathbf{F}_a) \circ \Theta_a^*] \circ \Theta_r^* \} \circ \Theta_s^* \rangle \mathbf{F}_a^H \Psi_a \quad (6)$$

$$\mathcal{T}(\mathbf{Y}) = \langle \mathbf{F}_r^H \{ \mathbf{F}_r [(\Psi_r^H \mathbf{Y} \Psi_a^H \mathbf{F}_a) \circ \Theta_s] \circ \Theta_r \} \circ \Theta_a \rangle \mathbf{F}_a^H \quad (7)$$

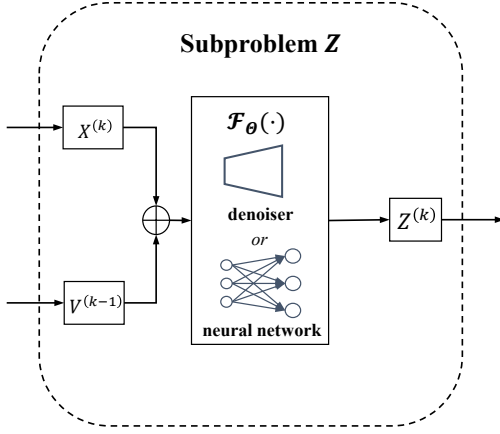


Fig. 3. Computational diagram of subproblem Z

where $\rho_n = \rho/L$ is the normalized penalty parameter, $\mu = 2/L$ is a step size parameter derived from the Lipschitz constant, and $\mathcal{T}(\cdot)$ denotes the imaging operator with down-sampling matrices, which can be formulated as Eq. 7.

2) *Subproblem Z*: Replacing the empirical regularizer (e.g., ℓ_1 -norm) with a function $\phi(\cdot)$, the nonlinear proximal operator $\mathcal{F}(\cdot)$ determined by $\phi(\cdot)$ is implemented through either model-based denoiser or data-driven neural networks. Consequently, the closed-form solution of subproblem Z is formulated as

$$\mathbf{Z}^{(k)} = \mathcal{F}_{\Theta}(\mathbf{X}^{(k)} + \mathbf{V}^{(k-1)}), \quad (12)$$

where $\mathcal{F}_{\Theta}(\cdot)$ is the nonlinear proximal operator, and Θ denotes the parameters of the denoiser or neural network.

The computational flowchart of Subproblem Z is illustrated in Fig. 3.

3) *enhanced 2D imaging model*: By integrating the solutions of these subproblems, we obtain an enhanced 2D SAR imaging model, formulated as:

$$\begin{cases} \mathbf{X} : \mathbf{X}^{(k)} = (1 - \rho_n)\mathbf{X}^{(k-1)} + \mu\mathcal{T}[\mathbf{Y}_d - \mathcal{G}(\mathbf{X}^{(k-1)})] \\ \quad + \rho_n(\mathbf{Z}^{(k-1)} - \mathbf{V}^{(k-1)}) \end{cases} \quad (13a)$$

$$\mathbf{Z} : \mathbf{Z}^{(k)} = \mathcal{F}_{\Theta}(\mathbf{X}^{(k)} + \mathbf{V}^{(k-1)}) \quad (13b)$$

$$\mathbf{V} : \mathbf{V}^{(k)} = \mathbf{V}^{(k-1)} + \mathbf{X}^{(k)} - \mathbf{Z}^{(k)} \quad (13c)$$

The 2D imaging model, built upon ADMM without matrix inversion, overcomes the computational bottlenecks of conventional imaging frameworks. This lays a foundation for the ARSAR-Net in the next section.

III. ARSAR-NET

Based on the enhanced 2D imaging model, we present a SAR imaging network with adaptive regularization, termed ARSAR-Net, along with two variants: ARSAR-Net Swift, designed for high imaging efficiency, and ARSAR-Net Pro, aimed at achieving superior image quality.

A. Network Architecture

In Sec. II-B, we developed an enhanced SAR imaging model. However, this iterative framework involves multiple hyperparameters that require manual tuning. In addition, the effectiveness of the regularization function can be compromised in complex scenes. To address these challenges, we unfold the iterative framework into a deep unfolding network, termed ARSAR-Net, where each layer strictly corresponds to an iteration step. Unlike conventional model-driven approaches, this network enables data-driven parameter optimization based on SAR echo data and corresponding ground truth images.

As illustrated in Fig. 4, ARSAR-Net uses 2D echo data \mathbf{Y}_d as input and outputs the scattering coefficient matrix $\mathbf{X}^{(N)}$ (where the magnitude matrix of scattering coefficients represents the SAR image). The network consists of N_s layers, each containing three differentiable modules which correspond to the three variables in the 2D imaging model. The differentiable modules are detailed as follows.

1) **Reconstruction Module**: This module, designed upon Eq. 13a, reconstructs the scattering coefficient matrix \mathbf{X} by replacing the matrix inversion operation with a linear computation. Specifically, CSA operators derived from the SAR system parameters enforce physical constraints following the imaging principles. The computational process of the module is:

$$\begin{aligned} \mathbf{X}^{(k)} = & (1 - \tilde{\rho})\mathbf{X}^{(k-1)} + \tilde{\mu}\mathcal{T}[\mathbf{Y}_d - \mathcal{G}(\mathbf{X}^{(k-1)})] \\ & + \tilde{\rho}(\mathbf{Z}^{(k-1)} - \mathbf{V}^{(k-1)}), \end{aligned} \quad (14)$$

where $\mathbf{X}^{(k-1)}$, $\mathbf{Z}^{(k-1)}$, $\mathbf{V}^{(k-1)}$ and \mathbf{Y}_d denote the input variables, $\mathbf{X}^{(k)}$ corresponds to the reconstructed output, and

- $\mathcal{T}(\cdot)$: Imaging operator derived from CSA;
- $\mathcal{G}(\cdot)$: Observation operator derived from CSA;
- $\tilde{\rho}$: Network-shared learnable penalty parameter.
- $\tilde{\mu}$: Network-shared learnable step size parameter.

2) **Adaptive Regularizer Module**: This module, derived from Eq. 13b, iteratively updates \mathbf{Z} . It employs a neural network to construct the nonlinear projection operator $\mathcal{F}_{\Theta}(\cdot)$ for regularization, as:

$$\mathbf{Z}^{(k)} = \mathcal{F}_{\Theta}(\mathbf{X}^{(k)} + \mathbf{V}^{(k-1)}), \quad (15)$$

where $\mathbf{X}^{(k)}$, $\mathbf{V}^{(k-1)}$ denote the input variables and $\mathbf{Z}^{(k)}$ the reconstructed output variable. The detailed implementation of $\mathcal{F}_{\Theta}(\cdot)$ will be presented in Sec. III-B.

3) **Scaled Multiplier Module**: This module updates the scaled dual variable \mathbf{V} by introducing a learnable, network-shared update rate $\tilde{\eta}$, which serves as an enhanced implementation of the standard formulation in Eq. 13c. This modification ensures stable convergence across network layers. The computational process is formulated as:

$$\mathbf{V}^{(k)} = \mathbf{V}^{(k-1)} + \tilde{\eta}(\mathbf{X}^{(k)} - \mathbf{Z}^{(k)}), \quad (16)$$

where $\mathbf{X}^{(k)}$, $\mathbf{Z}^{(k)}$, $\mathbf{V}^{(k-1)}$ denote the input variables, and $\mathbf{V}^{(k)}$ the updated scaled dual variable.

ARSAR-Net eliminates the need for manual parameter tuning through automated optimization across three key modules. Unlike conventional deep networks, it derives its architecture

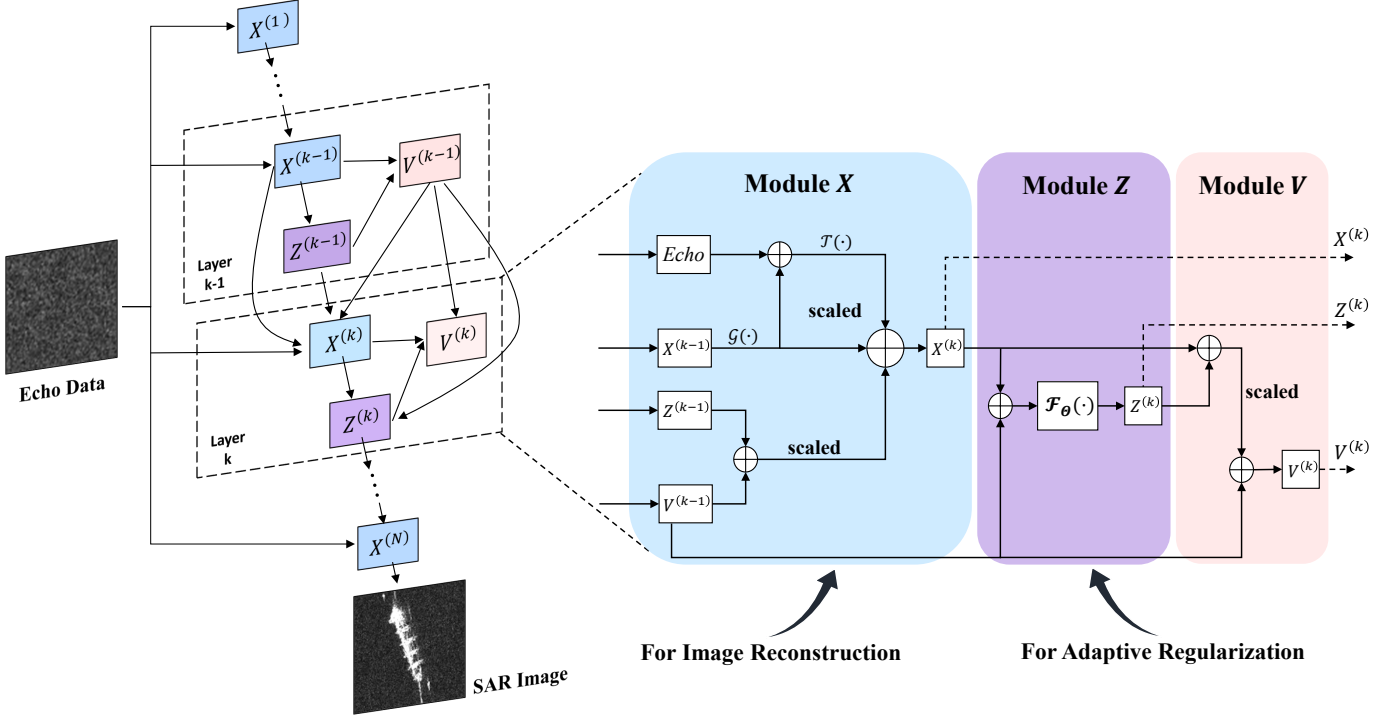


Fig. 4. Architecture of ARSAR-Net, which consists of a reconstruction module (\mathbf{X}), an adaptive regularizer module (\mathbf{Z}), and a scaled multiplier module (\mathbf{V}).

from the ADMM unfolding framework, offering improved interpretability and theoretical grounding.

B. Adaptive Regularizer

Given \mathbf{X} , \mathbf{Z} , and \mathbf{V} denoting 2D complex matrices in the network, ARSAR-Net employs specialized components for efficient complex-valued 2D data processing. The nonlinear projection operator \mathcal{F}_Θ in Eq. 15 is implemented through three components: convolutional layers for feature extraction, activation functions for inducing nonlinear mappings, and normalization layers for training stability.

As these components exclusively operate on real-valued data, we adopt a channel-expansion strategy by decomposing each complex matrix into separate real and imaginary channels. This changes the data dimensions from $[B, H, W]$ to $[B, C, H, W]$, where B is the batch size, H/W denotes spatial dimensions, and C denotes the channel dimension. The subsequent operation recombines the two separated channels, restoring the original $[B, H, W]$ dimensional structure.

We define two variants of ARSAR-Net: ARSAR-Net Swift for imaging efficiency and ARSAR-Net Pro for imaging quality³. As shown in Fig. 5, these variants use different architectures in the adaptive regularizer modules while sharing two core modules.

1) **ARSAR-Net Swift**: This module integrates a pyramid structure with multi-scale fusion blocks to reduce computational costs. The characteristics of this variant include:

- **Pyramid Structure**: As shown Fig. 5, this structure achieves feature map downsampling through two specialized convolutional modules. The first module, \mathcal{C}_1 , consists of a convolutional layer with a kernel size of 3, followed by batch normalization (BN) [48] and a ReLU activation function [49], specifically designed to reduce spatial resolution. The second module, \mathcal{C}_2 , employs a convolutional layer with a kernel size of 1 to expand the channel dimensions while preserving spatial resolution. The dimensional transformations in feature maps induced by these modules are as follows:

$$\begin{aligned} [B, C, H, W] &\xrightarrow{\mathcal{C}_1} [B, C, H/2, W/2] \\ [B, C, H/2, W/2] &\xrightarrow{\mathcal{C}_2} [B, 2C, H/2, W/2] \end{aligned}$$

- **Multi-scale Feature Fusion**: The multi-scale fusion block first applies interpolation-based upsampling to the downsampled feature maps, then concatenates them with the same-scale feature maps along the channel dimension. The fused features are then passed through the convolutional module \mathcal{C}_3 , which maintains spatial resolution while compressing channels. This process is expressed as

$$\begin{aligned} \sigma_{out}^{(i)} &= \text{Fusion}(\sigma^{(i)}, \sigma_{out}^{(i+1)}) = \mathcal{C}_3 [\sigma^{(i)} \oplus \text{Up}(\sigma_{out}^{(i+1)})] \\ [B, C, H/2, W/2] &\xrightarrow{\text{Up}} [B, C, H, W] \\ [B, 2C, H, W] &\xrightarrow{\mathcal{C}_3} [B, C, H, W] \end{aligned}$$

where $\sigma^{(i)}$ represents the i -th feature maps in the pyramidal structure, $\sigma_{out}^{(i)}$ denotes the i -th feature maps after

³Please refer to Appendix C for the complexity analysis of ARSAR-Net.

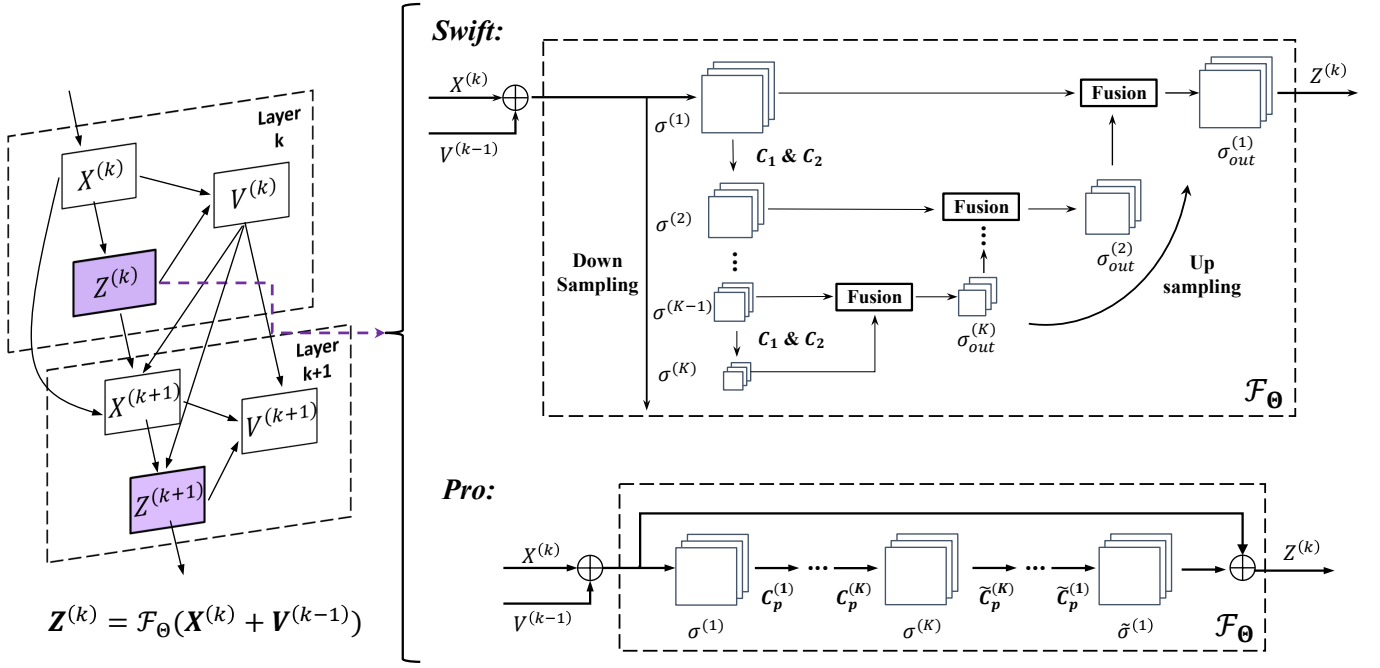


Fig. 5. Two variants of ARSAR-Net. ARSAR-Net Swift is specified for imaging efficiency, and ARSAR-Net Pro is specified for imaging quality.

upsampling, $Up(\cdot)$ refers to bilinear interpolation-based upsampling, and \oplus denotes channel-wise concatenation.

2) **ARSAR-Net Pro:** This module employs a symmetric architecture that maintains consistent feature resolution across network layers, enhancing detail preservation at the cost of computational efficiency. The main characteristics of this variant include:

- **Full-resolution Connectivity:** This variant maintains full-resolution feature propagation across all network layers, effectively mitigating the loss of image details. It also uses a convolutional cell \mathcal{C}_p composed of stacked convolutional layers with a kernel size of 3 and activation functions. This cell avoids feature map downsampling while progressively expanding channel dimensions. The dimensional transformation induced by the convolutional cell follows.

$$[B, C, H, W] \xrightarrow{\mathcal{C}_p} [B, 2C, H, W]$$

- **Symmetric Structural Module:** To ensure that the Adaptive Regularization Module's input and output have consistent channel dimensions, we construct a symmetric module $\tilde{\mathcal{C}}_p$ which mirrors the convolution cell. This mirrored module employs convolutional layers to reduce channel dimensions progressively. The dimensional transformation induced by the convolution module is as

$$[B, 2C, H, W] \xrightarrow{\tilde{\mathcal{C}}_p} [B, C, H, W]$$

- **Skip-connection Architecture:** This variant establishes an identity mapping, which allows gradients to flow directly through shortcut paths during training [50]. The Adaptive Regularization Module consists of K convolutional module pairs $\{\mathcal{C}_p^{(i)}, \tilde{\mathcal{C}}_p^{(i)}\}_{i=1}^K$, where each pair comprises

a convolutional cell $\mathcal{C}_p^{(i)}$ and its symmetric module $\tilde{\mathcal{C}}_p^{(i)}$. Collectively, these modules form the composite structure \mathcal{C}_{total} . We introduce skip-connections that establish an identity mapping external to \mathcal{C}_{total} structure, preserving details and accelerating network convergence. This design is formulated as

$$\begin{aligned} \mathcal{C}_{total} &= \mathcal{C}_p^{(1)} \mathcal{C}_p^{(2)} \dots \mathcal{C}_p^{(K)} \tilde{\mathcal{C}}_p^{(K)} \dots \tilde{\mathcal{C}}_p^{(2)} \tilde{\mathcal{C}}_p^{(1)} \\ \sigma_{final} &= \sigma^{(1)} + \tilde{\sigma}^{(1)} = \sigma^{(1)} + \mathcal{C}_{total}(\sigma^{(1)}) \end{aligned}$$

where $\sigma^{(1)}$ denote input feature maps, $\tilde{\sigma}^{(1)}$ feature maps after processing by \mathcal{C}_{total} and σ_{final} output feature maps.

C. Network Training

1) **Loss function:** The training dataset consists of N_{trn} samples, each defined as a pair (Y_i, X_i) , where Y_i represents a complex-valued SAR echo signal and X_i its corresponding ground truth image. Conventional loss functions, such as Mean Squared Error (MSE), exhibit disadvantages for complex-valued SAR image reconstruction. To bridge this gap, we introduce the Normalized Mean Perceived Error (NMPE), a specialized loss function designed to be both compatible with complex signals and computationally efficient, as

$$\mathcal{L} = \frac{1}{N_{trn}} \sum_{i=1}^{N_{trn}} \frac{\frac{1}{H \times W} \sum_{p=1}^H \sum_{q=1}^W (|\hat{X}_i(p, q)| - |X_i(p, q)|)^2}{\|X_i\|_2} \quad (17)$$

where \hat{X}_i and Y_i respectively denote ARSAR-Net's output and input, $\|\cdot\|_2$ denotes the ℓ_2 -norm.

2) **Training Configuration:** We implement ARSAR-Net in the PyTorch framework [51], using the Adam optimizer [52] with a learning rate of 2e-5 across 80 training epochs. Both variants of ARSAR-Net share identical configurations: a 9-layer architecture and a batch size of 4 during training.

TABLE I
MAIN PARAMETERS OF THE SAR SYSTEM

Parameter	Value
Signal bandwidth	60 MHz
Pulse width	45 us
Pulse repetition frequency	1420 Hz
Carrier frequency	5.4 GHz
Slant range	850 km
Equivalent velocity	7500 m/s

TABLE II
DATASET CONFIGURATION

Label	Training	Testing
Off-shore Ships	800	200
Harbors	400	100
Cities	400	100

IV. EXPERIMENT

In this section, we validate the superiority of ARSAR-Net upon both simulated and real data, through experiments on both simulated distributed targets (Sec. IV-B) and real data (Sec. IV-C). We also discuss the convergence rate of ARSAR-Net in Sec. IV-D.

A. Experimental Setting

1) *SAR System Parameters*: All the real SAR data used in the experiment are acquired from GaoFen-3, China's first C-band polarimetric SAR satellite, which supports 12 imaging modes and quad-polarization. Key parameters of this system are given in table I, which are also adopted in the generation of the simulated echo data.

2) *Experimental Platform*: All the experiments are conducted on a platform with an Intel Xeon Gold 5320 CPU (2.20 GHz) and NVIDIA A100-80GB GPU.

3) *Dataset*: For network training, we construct a dataset from SAR single-look complex (SLC) images at 1m resolution acquired by the Gaofen-3 satellite. This dataset consists of 2,000 images categorized into three distinct scenes: offshore ships, harbors, and cities. These data are divided into 1,600 training samples and 400 test samples, shown in Table II, with each image standardized to 512×512 pixels through cropping.

The CSA inverse imaging operator, configured using SAR system parameters from Table I, generates simulated echo signals that serve as network inputs, while the corresponding SLC images are used as ground truth. The range-direction sampling rate is constrained by the transmitted signal bandwidth, whereas the azimuth-direction sampling regulated by the pulse repetition frequency (PRF) offers greater operational flexibility [53]. This inherent characteristic renders azimuth downsampling particularly advantageous for practical implementation, compressing acquired information without compromising image quality. We utilize a random matrix as the downsampling matrix Ψ , which has been proven to meet the RIP conditions [54] [55]. Through random sampling, we generate azimuth-downsampled echoes at 50% and 75% of full sampling rates, which are subsequently used for network training and testing.

4) *Evaluation Metrics*: To quantitatively evaluate the performance of ARSAR-Net, the following evaluation metrics are employed: NRMSE [56], Peak Signal-to-Noise Ratio (PSNR, measured in dB), and Structural Similarity Index for Measuring (SSIM) [57] ⁴.

B. Distributed Target Simulation

Two simulation experiments are carried out to evaluate ARSAR-Net and compare it with representative methods, including the CSA-based method [44], ℓ_1 -Norm [58], and total variation (TV) regularization [59], as well as unfolding network-based methods (LRSR-ADMM-Net [36] and SR-CSA-Net [39]). Azimuth downsampling is an effective strategy for reducing data storage and transmission demands in the SAR system. In these experiments, the simulated echoes are azimuth-downsampled at two rates (50% and 75%) to assess imaging performance under varying sampling conditions, with quantitative results summarized in Table III. For a fair comparison, all methods use identical downsampled echo data under consistent experimental settings.

With 50% downsampling, shown in Fig. 6, all methods exhibit noticeable artifacts and ambiguity. Conventional methods, including CSA, ℓ_1 -Norm, and TV regularization, demonstrate suboptimal imaging performance, with lower PSNR and SSIM values, alongside higher NRMSE values, indicating significant deviations from the ground truth. These deviations are particularly apparent in the azimuth direction. LRSR-ADMM-Net shows poor performance, whereas SR-CSA-Net achieves moderate improvements. The visual results reveal partial suppression of azimuth ambiguities and enhanced edge definitions. The proposed ARSAR-Net Swift substantially improves imaging quality. It mitigates the azimuth ambiguity while recovering edge structures aligned with the ground truth. Notably, the ARSAR-Net Pro variant achieves state-of-the-art performance, with a PSNR of 24.54 dB, and SSIM of 0.862, preserving fine details and maintaining structural similarity up to 86% relative to ground truth.

Under the 75% downsampling condition, imaging performance improves across all methods. Conventional approaches exhibit moderate quality, yet still suffer from detail loss and azimuth ambiguity. Unfolding network-based methods, such as SR-CSA-Net, yield stronger imaging performance with fewer distortions and improved edge fidelity, reaching a PSNR value above 22.78 dB and an SSIM value exceeding 0.861. ARSAR-Net Swift delivers superior results, effectively suppressing ambiguities while recovering detailed structures. Meanwhile, ARSAR-Net Pro achieves the highest imaging quality, with a PSNR of 32.41 dB, and SSIM of 0.948, maintaining fine textures and overall structural consistency with the ground truth. Both variants demonstrate robust generalization and strong performance in preserving image fidelity.

C. Imaging in Real Scenes

1) *Overall dataset*: The first experiment is carried out on the overall dataset under two sampling rates (50% and

⁴Please refer to Appendix D for definitions of these evaluation metrics.

TABLE III
COMPARISON OF IMAGING PERFORMANCE UNDER SAMPLING RATES FOR SIMULATION SCENES

Method	50% Sampling Rate			75% Sampling Rate		
	NRMSE	PSNR	SSIM	NRMSE	PSNR	SSIM
CSA	0.605	12.52	0.424	0.460	14.99	0.485
ℓ_1 -Norm	0.521	14.16	0.574	0.203	20.04	0.791
TV	0.544	13.37	0.512	0.374	16.53	0.608
LRSR-ADMM-Net	0.722	11.32	0.375	0.418	15.61	0.491
SR-CSA-Net	0.209	20.24	0.683	0.159	22.78	0.861
ARSAR-Net Swift	0.239	18.83	0.685	0.086	28.17	0.861
ARSAR-Net Pro	0.140	24.54	0.862	0.047	32.41	0.948

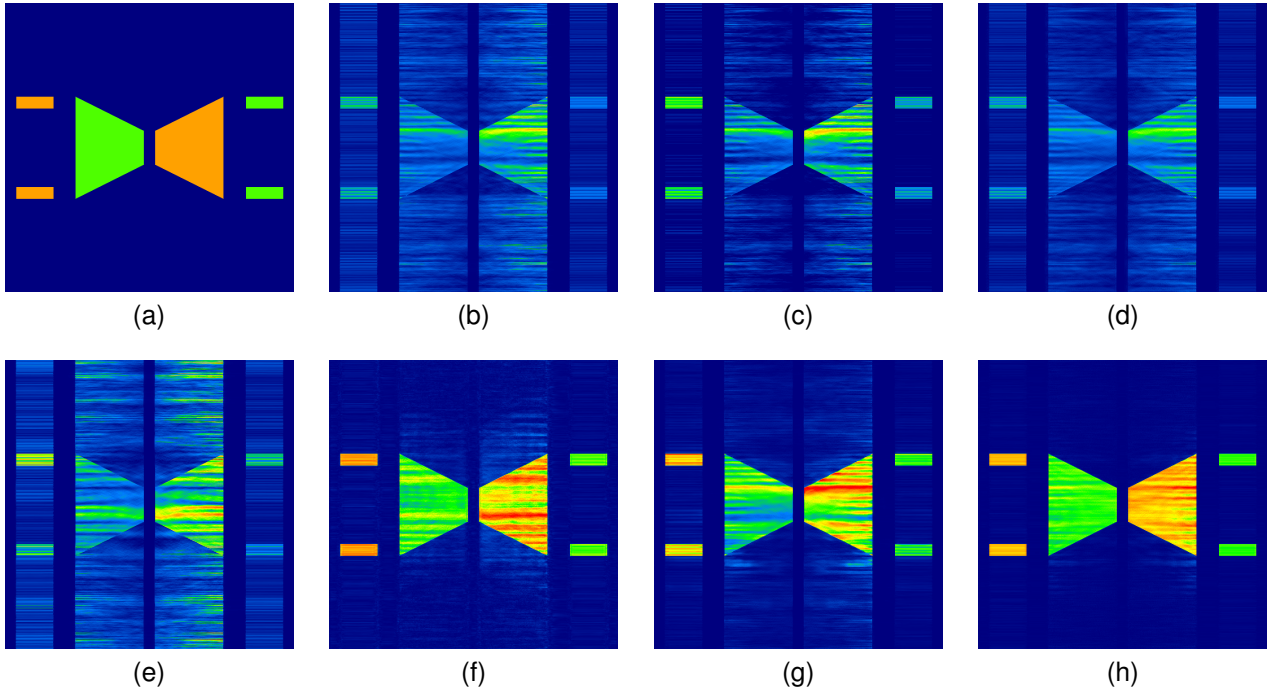


Fig. 6. Simulated scene results in different methods with 50% sampling rate. (a) ground truth. (b) CSA. (c) ℓ_1 -Norm. (d) TV. (e) LRSR-ADMM-Net. (f) SR-CSA-Net. (g) ARSAR-Net Swift. (h) ARSAR-Net Pro.

75%), comparing its performance against a range of conventional and unfolding network-based methods. The conventional methods include the CSA-based imaging operators method and regularization techniques such as ℓ_1 -norm and TV approaches. Among deep learning baselines, we include unfolding network-based methods like LRSR-ADMM-Net⁵ and SR-CSA-Net for a more comprehensive comparison. The overall dataset contains a diverse mix of real-world SAR scenes, covering both sparse and non-sparse scenes. Experimental results are included in Table IV.

In Fig. 7, reconstruction results suffer from the azimuth

⁵While LRSR-ADMM-Net demonstrated promising results in its original work [36], our evaluation reveals a noticeable performance gap in real-scene reconstruction. This is largely due to dataset variations between the two studies.

ambiguity under the 50% sampling rate. The CSA-based imaging operators (Fig. 7b) show limited capability in suppressing ambiguities. The TV regularization method (Fig. 7d) is effective at suppressing gradient variations induced by noise but experiences difficulty in handling more severe ambiguities. In contrast, the ℓ_1 -norm method (Fig. 7c) demonstrates better suppression of the ambiguity in sparse scenes due to its sparsity-promoting nature. However, it tends to eliminate a substantial amount of fine detail, resulting in compromised structural fidelity in non-sparse scenes. Unfolding networks enhance imaging quality in a data-driven fashion. LRSR-ADMM-Net and SR-CSA-Net (Figs. 7e and 7f) show moderate improvements, achieving better suppression of azimuth ambiguities while preserving structural details. The proposed ARSAR-Net Swift (Fig. 7g) demonstrates high imaging qual-

TABLE IV
COMPARISON OF IMAGING PERFORMANCE UNDER SAMPLING RATES FOR REAL SCENES

Method	50% Sampling Rate			75% Sampling Rate			Imaging Speed (items/s)
	NRMSE	PSNR	SSIM	NRMSE	PSNR	SSIM	
CSA	0.384	24.02	0.539	0.287	26.78	0.693	210.2
ℓ_1 -Norm	0.675	22.79	0.286	0.676	24.01	0.318	3.656
TV	0.377	24.07	0.550	0.276	26.36	0.694	3.371
LRSR-ADMM-Net	0.349	24.11	0.543	0.186	27.00	0.688	1.947
SR-CSA-Net	0.162	28.91	0.756	0.077	34.17	0.903	43.84
ARSAR-Net Swift	0.089	29.15	0.743	0.062	33.29	0.881	67.60
ARSAR-Net Pro	0.084	30.75	0.810	0.036	36.05	0.928	17.60

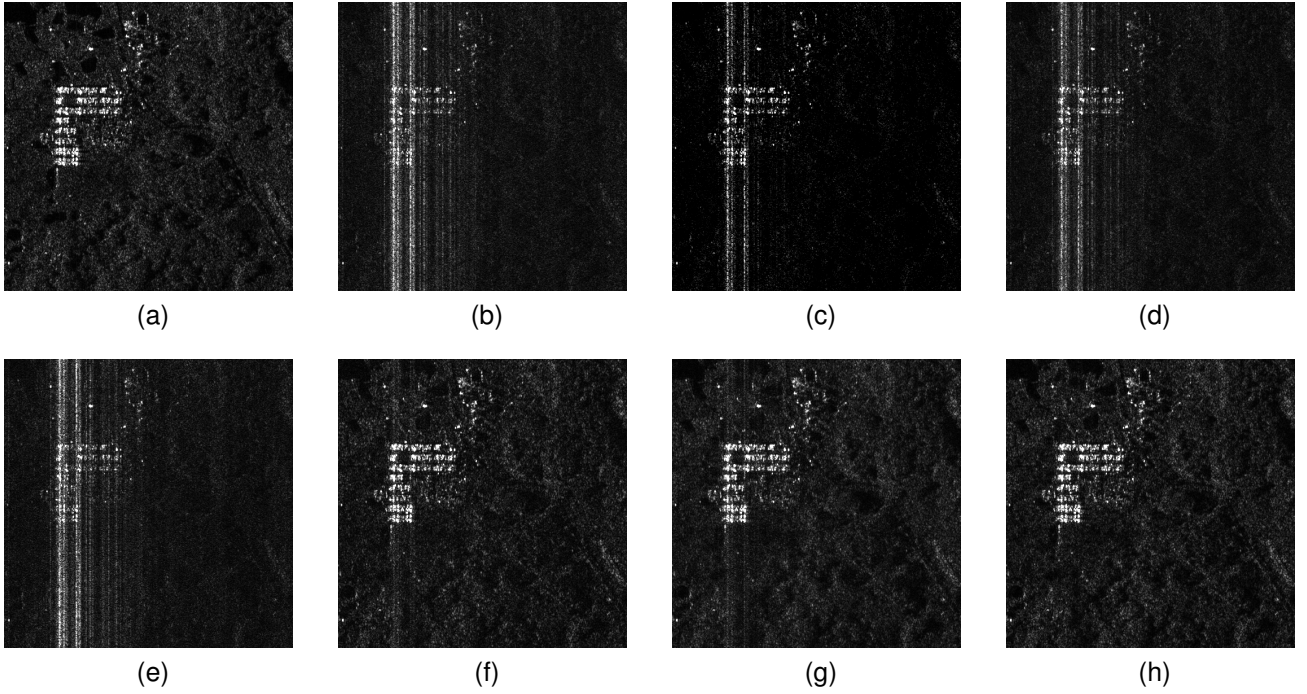


Fig. 7. Real sparse scene results in different methods with 50% sampling rate. (a) ground truth. (b) CSA. (c) ℓ_1 -Norm. (d) TV. (e) LRSR-ADMM-Net. (f) SR-CSA-Net. (g) ARSAR-Net Swift. (h) ARSAR-Net Pro.

ity across different scene types. However, the use of downsampling operations in the feature extraction stage inevitably leads to the loss of fine details. ARSAR-Net Pro (Fig. 7h) achieves superior performance, with a PSNR of 30.75 dB, and SSIM of 0.810, outperforming other methods with large margins.

The azimuth ambiguity is significantly reduced under the 75% sampling rate, leading to noticeable improvements in image quality, shown in Fig. 8. Conventional methods (Figs. 8b, 8c and 8d) show moderate enhancement compared to the 50% case, but shortcomings such as detail loss and residual ambiguities remain apparent. SR-CSA-Net, ARSAR-Net Swift, and ARSAR-Net Pro deliver high reconstruction quality under the 75% sampling rate. Notably, ARSAR-Net Pro (Fig. 8h) achieves state-of-the-art performance, attaining a PSNR of 36.05 dB and SSIM of 0.928, while maintaining fine textures and robust structural consistency.

Imaging speed is an important factor in practical systems. While the CSA-based imaging operators attain the highest imaging speed of 210.2 items/s, they suffer from low image quality. Conventional approaches suffer from low efficiency due to their iterative optimization procedures requiring repeated updates. The unfolding network, LRSR-ADMM-Net, is bottlenecked by the singular value decomposition operations, whereas SR-CSA-Net achieves faster reconstruction through its deep unfolding architecture. Our ARSAR-Net Swift further optimizes efficiency with a pyramid-structured network, achieving a superior imaging speed of 67.60 items/s. ARSAR-Net Pro prioritizes reconstruction fidelity through a full-resolution architecture, delivering the highest precision at the cost of efficiency.

2) *Subsets about sparse and non-sparse scenes:* This experiment assesses adaptability in scenes of different sparsity. The

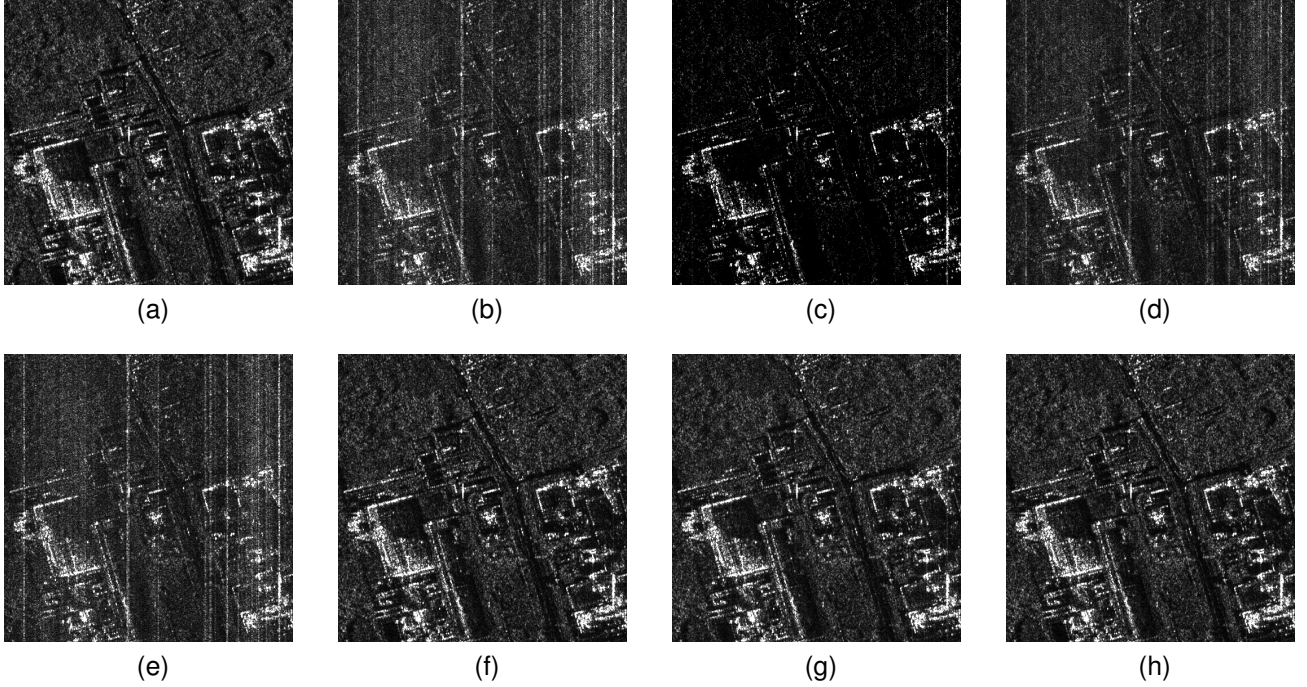


Fig. 8. Real non-sparse scene results in different methods with 75% sampling rate. (a) ground truth. (b) CSA. (c) ℓ_1 -Norm. (d) TV. (e) LRSR-ADMM-Net. (f) SR-CSA-Net. (g) ARSAR-Net Swift. (h) ARSAR-Net Pro.

TABLE V
COMPARISON OF IMAGING PERFORMANCE UNDER SAMPLING RATES IN SUBSETS

Scene Type	Method	50% Sampling Rate			75% Sampling Rate		
		NRMSE	PSNR	SSIM	NRMSE	PSNR	SSIM
Sparse	ℓ_1 -Norm	0.747	29.21	0.319	0.752	29.91	0.330
	LRSR-ADMM-Net	0.334	31.23	0.746	0.173	34.27	0.853
	SR-CSA-Net	0.278	32.91	0.777	0.147	35.98	0.877
	ARSAR-Net	0.134	34.60	0.802	0.056	37.93	0.902
Non-sparse	ℓ_1 -Norm	0.615	18.24	0.277	0.611	19.93	0.328
	LRSR-ADMM-Net	0.355	19.07	0.397	0.191	21.89	0.567
	SR-CSA-Net	0.086	26.00	0.743	0.031	32.78	0.921
	ARSAR-Net	0.050	28.01	0.817	0.023	34.65	0.947

compared approaches consist of a conventional method based on ℓ_1 -norm and two unfolding networks: LRSR-ADMM-Net and SR-CSA-Net. To ensure a fair comparison, all data-driven methods are trained on the overall dataset. A summary of experimental results is provided in Table V. For the case of the 50% sampling rate, Fig. 9 and Fig. 10 illustrate the visual imaging results in sparse and non-sparse scenes, respectively.

The conventional method based on ℓ_1 -norm regularization shows strong noise and ambiguity suppression capabilities, but it suffers from a significant loss of image details. In simple sparse scenes, this approach performs poorly compared to unfolding network-based methods, with a PSNR drop of about 5.5 dB and an SSIM reduction of around 0.5. The detail loss becomes even more severe in complex non-sparse scenes, leading to a more substantial reduction of 10 dB in

PSNR and 0.55 in SSIM compared to the best-performing method. Such significant declines in reconstruction accuracy render the ℓ_1 -norm method inadequate for SAR imaging under downsampled conditions.

LRSR-ADMM-Net achieves promising imaging quality in sparse scenes, with PSNR and SSIM values comparable to the best-performing method. Nevertheless, due to its limited parameter size and training capacity, its performance degrades in non-sparse scenes, e.g., PSNR dropping by about 9 dB and SSIM decreasing by 0.4 compared to ARSAR-Net. This substantial performance gap indicates that LRSR-ADMM-Net lacks the adaptability to non-sparse scenes. By integrating an unfolding network with the CSA-based imaging operators, SR-CSA-Net achieves high imaging performance in both sparse and non-sparse scenes. The proposed ARSAR-Net further

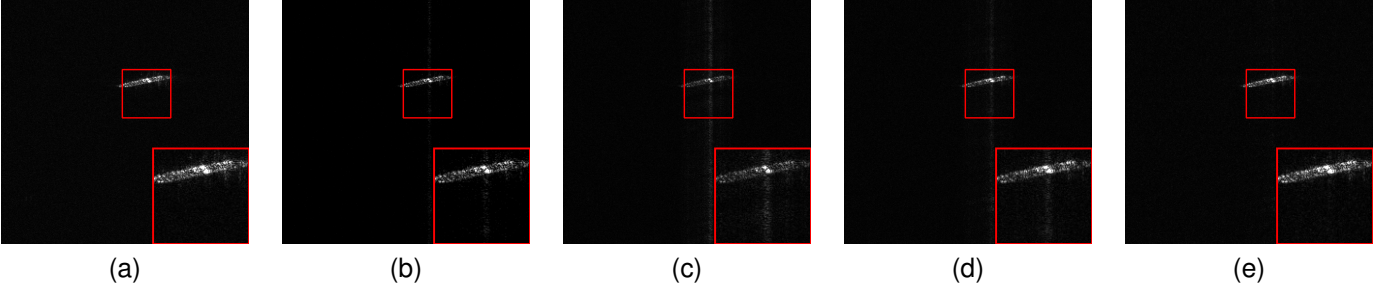


Fig. 9. Comparison of imaging results in a sparse scene. (a) ground truth. (b) ℓ_1 -Norm. (c) LRSR-ADMM-Net. (d) SR-CSA-Net. (e) ARSAR-Net.

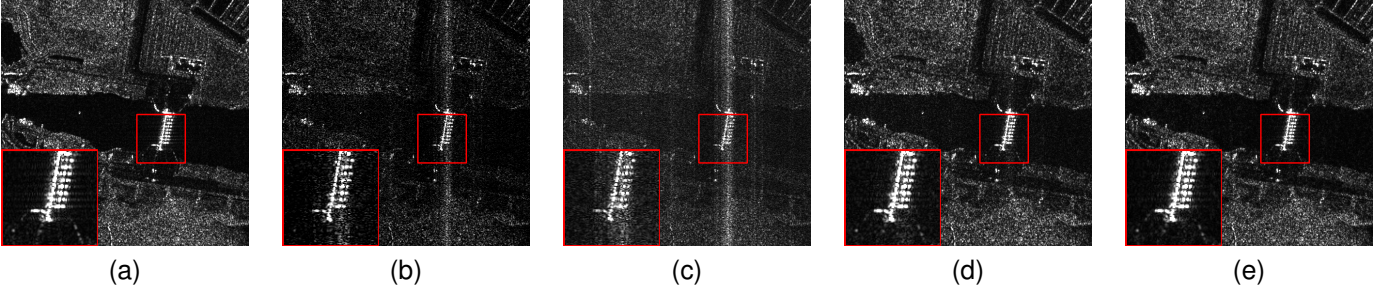


Fig. 10. Comparison of imaging results in a non-sparse scene. (a) ground truth. (b) ℓ_1 -Norm. (c) LRSR-ADMM-Net. (d) SR-CSA-Net. (e) ARSAR-Net.

improves reconstruction fidelity through the adaptive regularizer module, outperforming existing methods by 2 dB PSNR. These results validate its generalization capacity across scenes.

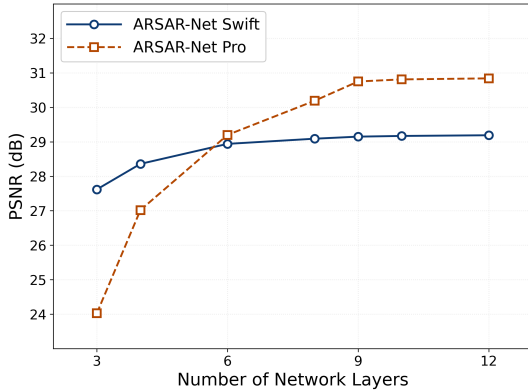


Fig. 11. PSNR under different layers

3) *Network Layers setting*: ARSAR-Net is derived by unfolding the ADMM algorithm without matrix inversion, where each layer corresponds to an iteration. Therefore, the number of network layers N_s has a significant impact on both imaging speed (items/s) and reconstruction quality, which is summarized in Table VI.

In Fig. 12, the PSNR value of ARSAR-Net Swift increases gradually with network layers and begins to plateau around 29.2 dB when the depth exceeds 9. In contrast, ARSAR-Net Pro shows a sharp improvement in PSNR as the depth increases, eventually stabilizing at about 30.8 dB beyond 8 layers. On the other hand, the imaging speed of both variants decreases rapidly as the number of layers increases.

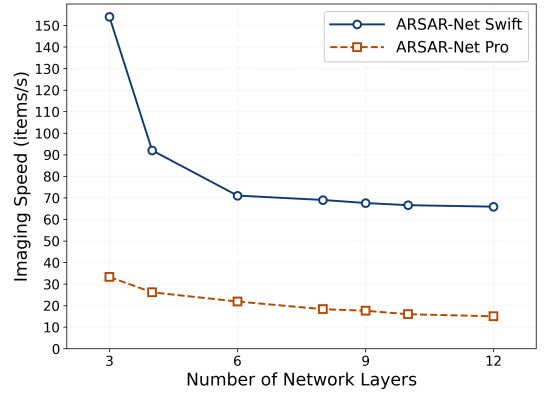


Fig. 12. Imaging speed under different layers

For the trade-off between quality and speed, we select a 9-layer network for both ARSAR-Net variants. This shows superior imaging performance compared to networks with fewer layers while maintaining high imaging efficiency.

As shown in Fig. 13, the outputs of ARSAR-Net Pro from layers 1, 3, 5, 7, and 9 demonstrate a progressive improvement in reconstruction quality under a 50% sampling rate.

D. Training Convergence

During training, the compared unfolding networks demonstrate different convergence behaviors, illustrated in Fig. 14. LRSR-ADMM-Net exhibits a relatively flat and stable loss curve throughout training, indicating constrained adaptability due to the limited size of its trainable parameters. In contrast, SR-CSA-Net achieves rapid convergence in the early epochs, with its loss decreasing from over 4.6 to 1.2 before stabilizing.

TABLE VI
PERFORMANCE OF ARSAR-NET VARIANTS UNDER DIFFERENT LAYER NUMBERS UNDER 50% DOWNSAMPLING RATE

Method	$N_s = 3$			$N_s = 6$			$N_s = 9$		
	PSNR	SSIM	Speed	PSNR	SSIM	Speed	PSNR	SSIM	Speed
ARSAR-Net Swift	28.64	0.728	154.0	28.99	0.739	71.23	29.15	0.743	67.60
ARSAR-Net Pro	24.03	0.540	33.28	29.20	0.783	21.92	30.75	0.810	17.60

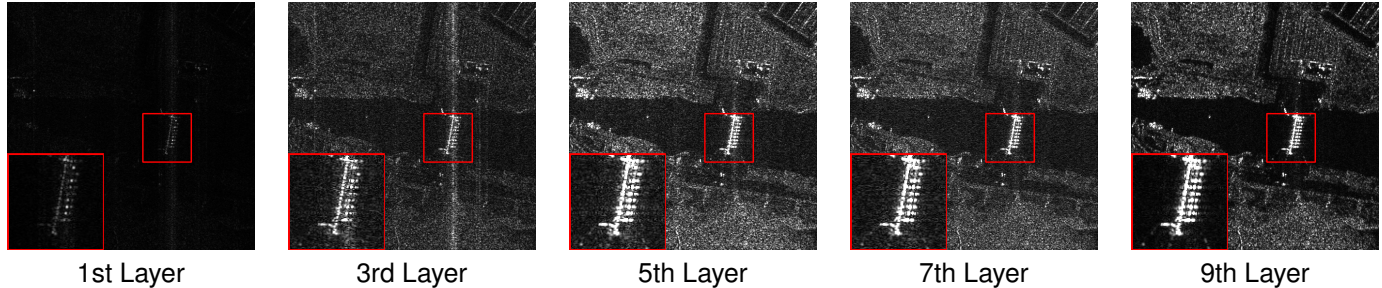


Fig. 13. Reconstruction results of ARSAR-Net Pro at different layers under 50% sampling rate.

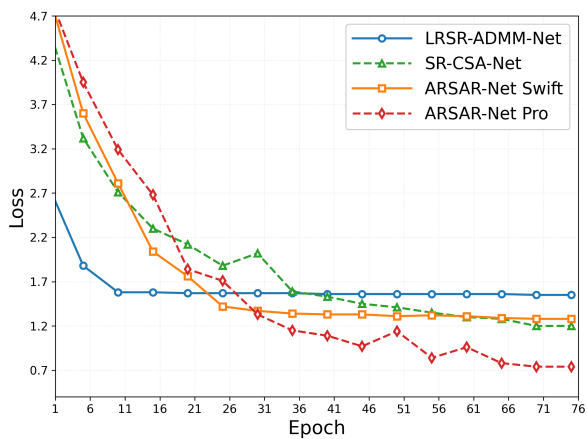


Fig. 14. Training loss curves of compared methods

This smooth convergence suggests strong learning capability, particularly during the early stages of training.

Meanwhile, ARSAR-Net Swift starts with the highest initial loss among all methods but shows a steady decline, indicating a stable training process with consistent improvements. While it does not achieve as low a final loss as ARSAR-Net Pro, its convergence trend remains reliable. ARSAR-Net Pro, by contrast, reaches the lowest loss (around 0.7), demonstrating strong optimization capability and superior training efficiency.

Overall, ARSAR-Net Pro enjoys the best convergence performance, achieving a balance between speed and final loss. In comparison, ARSAR-Net Swift converges more gradually, reflecting a stable and robust optimization process.

V. CONCLUSION

We proposed ARSAR-Net, a SAR imaging network with adaptive regularization, to address the limited generalization

capability of baseline unfolding networks across heterogeneous scenes. By integrating a learnable regularization module into an unfolding architecture, ARSAR-Net enables adaptive and data-driven reconstruction across diverse environments such as offshore, urban, and mountainous areas. Built upon an enhanced imaging model derived from a matrix-inversion-free variant of ADMM, the network maintains computational efficiency while improving flexibility. To further meet application-specific needs, two variants of ARSAR-Net were introduced: ARSAR-Net Swift for accelerated imaging and ARSAR-Net Pro for high-fidelity reconstruction. Extensive experiments on both simulated and real SAR datasets validate the effectiveness of our approach, demonstrating significant gains in speed, image quality, and scene adaptability. The proposed framework advances SAR imaging by integrating model-driven priors with data-driven adaptability, providing fresh insight for high-quality and efficient SAR imaging in complex scenes.

APPENDIX A

ANALYSIS OF LIPSCHITZ CONTINUOUS CONDITION

We start by considering the expression of the objective function $\mathcal{S}(\mathbf{X})$, which consists of a data fidelity term involving the observation operator $\mathcal{G}(\cdot)$, and several quadratic terms:

$$\begin{aligned} \mathcal{S}(\mathbf{X}^{(k)}) = & \left\| \mathcal{G}(\mathbf{X}^{(k)}) - \mathbf{Y}_d \right\|_2^2 \\ & + \frac{\rho}{2} \left\| \mathbf{X}^{(k)} - \mathbf{Z}^{(k-1)} + \mathbf{V}^{(k-1)} \right\|_2^2. \end{aligned}$$

The quadratic terms possess constant second-order derivatives, and therefore naturally satisfy the Lipschitz continuity condition. The Lipschitz continuity of the Hessian of $\mathcal{S}(\mathbf{X})$ is primarily determined by the characteristics of the observation operator $\mathcal{G}(\cdot)$, which consists of three components: Fourier transforms, downsampling matrices, and Hadamard products. The contribution of each component is analyzed individually below.

- **Fourier Transform:** This is a linear and unitary operation. Its derivative (Jacobian) is constant, and its second derivative (Hessian) is zero. Therefore, it satisfies the Lipschitz continuity condition trivially.
- **Downsampling Matrix:** The downsampling matrix used here performs random row selection from a full-size identity matrix, forming a binary selection operator. As a linear projection, it introduces no nonlinearity, thereby trivially satisfying the Lipschitz continuity condition.
- **Hadamard Product:** Since the element-wise (Hadamard) product is applied with a constant matrix determined by radar system parameters, the operation is strictly linear and equivalent to a diagonal linear operator. As such, the operator admits constant first-order and second-order derivatives, thereby satisfying the Lipschitz continuity condition for the Hessian.

Therefore, there exists a Lipschitz constant $L > 0$ such that for any \mathbf{X} and $\mathbf{X}^{(k-1)}$,

$$\left\| \nabla^2 S(\mathbf{X}) - \nabla^2 S(\mathbf{X}^{(k-1)}) \right\| \leq L \left\| \mathbf{X} - \mathbf{X}^{(k-1)} \right\|.$$

Since the Hessian of $S(\mathbf{X})$ is Lipschitz continuous, its variation is bounded within a local neighborhood. When \mathbf{X} is sufficiently close to $\mathbf{X}^{(k-1)}$, we have

$$\nabla^2 S(\mathbf{X}^{(k-1)}) \left\| \mathbf{X} - \mathbf{X}^{(k-1)} \right\| \leq L \left\| \mathbf{X} - \mathbf{X}^{(k-1)} \right\|.$$

In practical implementations, we adopt this estimated upper bound L to approximate the second-order behavior of the objective function and derive Eq. 10 accordingly.

APPENDIX B PROOF OF EQ. 11

Eq. 10 is to be simplified as follows.

$$\mathbf{X}^{(k)} = \arg \min_{\mathbf{X}} [S(\mathbf{X}^{(k-1)}) + \nabla S(\mathbf{X}^{(k-1)})^H (\mathbf{X} - \mathbf{X}^{(k-1)}) + \frac{L}{2} \left\| \mathbf{X} - \mathbf{X}^{(k-1)} \right\|_2^2]$$

We combine the linear and quadratic terms by completing the square, as shown in the following equation.

$$\begin{aligned} \mathbf{X}^{(k)} = \arg \min_{\mathbf{X}} [& S(\mathbf{X}^{(k-1)}) + \nabla S(\mathbf{X}^{(k-1)})^H (\mathbf{X} - \mathbf{X}^{(k-1)}) \\ & + \frac{L}{2} \left\| \mathbf{X} - \mathbf{X}^{(k-1)} \right\|_2^2 \\ & - \frac{1}{2L} \nabla S(\mathbf{X}^{(k-1)})^H \nabla S(\mathbf{X}^{(k-1)}) \\ & + \frac{1}{2L} \nabla S(\mathbf{X}^{(k-1)})^H \nabla S(\mathbf{X}^{(k-1)})] \end{aligned} \quad (18)$$

After simplification, we obtain the following result:

$$\begin{aligned} \mathbf{X}^{(k)} = \arg \min_{\mathbf{X}} [& \frac{L}{2} \left\| \mathbf{X} - \mathbf{X}^{(k-1)} + \frac{1}{L} \nabla S(\mathbf{X}^{(k-1)}) \right\|_2^2 \\ & + S(\mathbf{X}^{(k-1)}) - \frac{1}{2L} \nabla S(\mathbf{X}^{(k-1)})^H \nabla S(\mathbf{X}^{(k-1)})]. \end{aligned} \quad (19)$$

where $S(\mathbf{X}^{(k-1)})$, $\frac{1}{2L} \nabla S(\mathbf{X}^{(k-1)})^H \nabla S(\mathbf{X}^{(k-1)})$ are constant terms irrelevant to the optimization variable \mathbf{X} .

The constant terms independent of \mathbf{X} are omitted, as it does not affect the minimization, as

$$\mathbf{X}^{(k)} = \arg \min_{\mathbf{X}} \frac{L}{2} \left\| \mathbf{X} - \mathbf{X}^{(k-1)} + \frac{1}{L} \nabla S(\mathbf{X}^{(k-1)}) \right\|_2^2. \quad (20)$$

By solving the minimization problem, we obtain an iterative solution in the form of a gradient descent step, as

$$\mathbf{X}^{(k)} = \mathbf{X}^{(k-1)} - \frac{1}{L} \nabla S(\mathbf{X}^{(k-1)}). \quad (21)$$

The gradient of the objective function $S(\mathbf{X})$ is computed as follows. Since both $\mathcal{G}(\cdot)$ and $\mathcal{T}(\cdot)$ are composed entirely of linear operations, they form a conjugate transpose pair [39], i.e.,

$$\mathcal{G}^H(\cdot) = \mathcal{T}(\cdot).$$

As a result, the first-order derivative (gradient) of $\mathcal{G}(\cdot)$ is given by $\mathcal{T}(\cdot)$, which simplifies the gradient expression.

$$\begin{aligned} \nabla S(\mathbf{X}^{(k)}) &= \nabla \left\| \mathcal{G}(\mathbf{X}^{(k)}) - \mathbf{Y}_d \right\|_2^2 \\ &+ \frac{\rho}{2} \nabla \left\| \mathbf{X}^{(k)} - \mathbf{Z}^{(k-1)} + \mathbf{V}^{(k-1)} \right\|_2^2 \\ &= 2\mathcal{G}^H[\mathcal{G}(\mathbf{X}^{(k)}) - \mathbf{Y}_d] \\ &+ \rho(\mathbf{X}^{(k)} - \mathbf{Z}^{(k-1)} + \mathbf{V}^{(k-1)}) \\ &= 2\mathcal{T}[\mathcal{G}(\mathbf{X}^{(k)}) - \mathbf{Y}_d] \\ &+ \rho(\mathbf{X}^{(k)} - \mathbf{Z}^{(k-1)} + \mathbf{V}^{(k-1)}), \end{aligned} \quad (22)$$

where the imaging operator $\mathcal{T}(\cdot)$ is given by Eq. 7.

Substituting the gradient expression into the iterative solution, we have

$$\begin{aligned} \mathbf{X}^{(k)} &= \mathbf{X}^{(k-1)} - \frac{2}{L} \mathcal{T}[\mathcal{G}(\mathbf{X}^{(k-1)}) - \mathbf{Y}_d] \\ &- \frac{\rho}{L} (\mathbf{X}^{(k-1)} - \mathbf{Z}^{(k-1)} + \mathbf{V}^{(k-1)}) \\ &= (1 - \frac{\rho}{L}) \mathbf{X}^{(k-1)} + \frac{2}{L} \mathcal{T}[\mathbf{Y}_d - \mathcal{G}(\mathbf{X}^{(k-1)})] \\ &+ \frac{\rho}{L} (\mathbf{Z}^{(k-1)} - \mathbf{V}^{(k-1)}). \end{aligned} \quad (23)$$

By redefining the parameters, the iterative solution can be simplified as follows, combining the previous estimate, the imaging residual, and the auxiliary variables:

$$\begin{aligned} \mathbf{X}^{(k)} &= (1 - \rho_n) \mathbf{X}^{(k-1)} + \mu \mathcal{T}[\mathbf{Y}_d - \mathcal{G}(\mathbf{X}^{(k-1)})] \\ &+ \rho_n (\mathbf{Z}^{(k-1)} - \mathbf{V}^{(k-1)}). \end{aligned}$$

APPENDIX C COMPLEXITY ANALYSIS

Each layer of ARSAR-Net consists of three modules: a reconstruction module, an adaptive regularizer module, and the scaled multiplier module. The scaled multiplier module, based on linear computations, has low computational complexity. Therefore, we focus on analyzing the complexity of the other two modules.

Let us assume that the scattering coefficient matrix \mathbf{X} is of size $N \times N$. According to Eq. 14, this module involves linear operations, the imaging operator \mathcal{T} , and the observation operator \mathcal{G} , as defined in Eq. 7 and Eq. 6, respectively. These

operators mainly consist of Fourier transforms and element-wise matrix multiplications (Hadamard products). The computational complexity of a two-dimensional Fourier transform is $\mathcal{O}(N^2 \log N)$ [60], while the complexity of element-wise matrix multiplication is $\mathcal{O}(N^2)$. Combining both operations, the overall complexity of this Module is

$$\mathcal{O}(N^2 \log N) + \mathcal{O}(N^2) = \mathcal{O}(N^2 \log N).$$

In the conventional ADMM algorithm, the computational bottleneck is matrix inversion, which has a complexity of $\mathcal{O}(N^3)$. By adopting the ADMM algorithm without matrix inversion, the reconstruction module reduces the complexity from $\mathcal{O}(N^3)$ to $\mathcal{O}(N^2 \log N)$.

As described in Sec. III-B, ARSAR-Net consists of two variants, Swift and Pro, which differ in the architecture of their adaptive regularizer modules.

For the adaptive regularizer module in the Swift variant, the main burden arises from convolutional layers. The complexity of the convolutional operation is $\mathcal{O}(N^2 \times C_{in} \times C_{out} \times K^2)$, where C_{in} denotes the number of input feature channels, C_{out} denotes the number of output feature channels and K the convolution kernel size. With the kernel size K being negligible relative to the feature map size N , the convolution operation has a simplified complexity denoted as $\mathcal{O}(N^2 \times C_{in} \times C_{out})$. Although the convolutional layers increase the number of feature channels, the size of feature maps is reduced at the same rate, keeping the overall complexity $\mathcal{O}(N^2)$. In contrast, this module in the Pro variant retains a full-resolution structure. While the size of feature maps remains fixed, the number of channels increases progressively. When the number of channels reaches its maximum, the input and output channels satisfy $C_{in} \times C_{out} \sim N$. Therefore, the complexity of this module is

$$\mathcal{O}(N^2 \times C_{in} \times C_{out}) = \mathcal{O}(N^3).$$

Since the modules in ARSAR-Net are executed sequentially, the overall complexity is determined by the module with the highest complexity. Consequently, the computational complexity of ARSAR-Net Swift is

$$\mathcal{O}(N^2 \log N) + \mathcal{O}(N^2) = \mathcal{O}(N^2 \log N),$$

while that of ARSAR-Net Pro is

$$\mathcal{O}(N^2 \log N) + \mathcal{O}(N^3) = \mathcal{O}(N^3).$$

APPENDIX D

DEFINITION OF EVALUATION METRICS

Let \hat{X} denote the reconstructed SAR image and X the ground truth. The mathematical formulations of these evaluation metrics are:

$$\text{NRMSE} = \frac{\sum_{i=1}^H \sum_{j=1}^W \|X(i, j) - \hat{X}(i, j)\|_2}{\sum_{i=1}^H \sum_{j=1}^W \|X(i, j)\|_2} \quad (24)$$

$$\text{PSNR} = 10 \log_{10} \left(\frac{\max_{1 \leq i \leq H, 1 \leq j \leq W} X(i, j)}{\frac{1}{N} \sum_{i=1}^H \sum_{j=1}^W (X(i, j) - \hat{X}(i, j))^2} \right) \quad (25)$$

$$\text{SSIM} = \frac{(2\mu_X \mu_{\hat{X}} + C_1)(2\sigma_{X\hat{X}} + C_2)}{(\mu_X^2 + \mu_{\hat{X}}^2 + C_1)(\sigma_X^2 + \sigma_{\hat{X}}^2 + C_2)}, \quad (26)$$

where X is the ground truth SAR image of size $H \times W$, \hat{X} is the reconstructed image of size $H \times W$, $N = H \times W$ is the total pixel count. $\mu_X = \frac{1}{N} \sum_{i=1}^N X_i$ and $\mu_{\hat{X}} = \frac{1}{N} \sum_{i=1}^N \hat{X}_i$ denote local pixel means; $\sigma_X^2 = \frac{1}{N-1} \sum_{i=1}^N (X_i - \mu_X)^2$ and $\sigma_{\hat{X}}^2 = \frac{1}{N-1} \sum_{i=1}^N (\hat{X}_i - \mu_{\hat{X}})^2$ denote standard deviations; $\sigma_{X\hat{X}} = \frac{1}{N-1} \sum_{i=1}^N (X_i - \mu_X)(\hat{X}_i - \mu_{\hat{X}})$ is cross-covariance; $C_1 = (K_1 L)^2$, $C_2 = (K_2 L)^2$, and L is the pixel value range and equals 255 for 8-bit grayscale images. In the experiment, we set $K_1 = 0.01$ and $K_2 = 0.03$.

REFERENCES

- [1] I. G. Cumming and F. H. Wong, "Digital processing of synthetic aperture radar data," *Artech house*, vol. 1, no. 3, pp. 108–110, 2005.
- [2] A. Moreira, P. Prats-Iraola, M. Younis, G. Krieger, I. Hajnsek, and K. P. Papathanassiou, "A tutorial on synthetic aperture radar," *IEEE Geoscience and remote sensing magazine*, vol. 1, no. 1, pp. 6–43, 2013.
- [3] R. P. Perry, R. C. DiPietro, and R. L. Fante, "Sar imaging of moving targets," *IEEE Transactions on Aerospace and Electronic Systems*, vol. 35, no. 1, pp. 188–200, 2002.
- [4] M. Çetin, I. Stojanović, N. Ö. Önhon, *et al.*, "Sparsity-driven synthetic aperture radar imaging: Reconstruction, autofocus, moving targets, and compressed sensing," *IEEE Signal Processing Magazine*, vol. 31, no. 4, pp. 27–40, 2014.
- [5] I. G. Cumming and S. Li, "Improved slope estimation for sar doppler ambiguity resolution," *IEEE transactions on geoscience and remote sensing*, vol. 44, no. 3, pp. 707–718, 2006.
- [6] G. O. Glentis, K. Zhao, A. Jakobsson, and J. Li, "Non-parametric high-resolution sar imaging," *IEEE Transactions on Signal Processing*, vol. 61, no. 7, pp. 1614–1624, 2012.
- [7] R. Bamler, "A comparison of range-doppler and wavenumber domain sar focusing algorithms," *IEEE Transactions on Geoscience and Remote Sensing*, vol. 30, no. 4, pp. 706–713, 1992.
- [8] R. K. Raney, H. Runge, R. Bamler, I. G. Cumming, and F. H. Wong, "Precision sar processing using chirp scaling," *IEEE Transactions on geoscience and remote sensing*, vol. 32, no. 4, pp. 786–799, 1994.
- [9] Z. Jin, Z. Pan, Z. Zhang, and X. Qiu, "Saas-net: Self-supervised sparse synthetic aperture radar imaging network with azimuth ambiguity suppression.," *Remote Sensing*, vol. 17, no. 6, 2025.
- [10] V. Monga, Y. Li, and Y. C. Eldar, "Algorithm unrolling: Interpretable, efficient deep learning for signal and image processing," *IEEE Signal Processing Magazine*, vol. 38, no. 2, pp. 18–44, 2021.

- [11] I. Daubechies, M. Defrise, and C. De Mol, "An iterative thresholding algorithm for linear inverse problems with a sparsity constraint," *Communications on Pure and Applied Mathematics: A Journal Issued by the Courant Institute of Mathematical Sciences*, vol. 57, no. 11, pp. 1413–1457, 2004.
- [12] S. Boyd, N. Parikh, E. Chu, B. Peleato, J. Eckstein, *et al.*, "Distributed optimization and statistical learning via the alternating direction method of multipliers," *Foundations and Trends® in Machine learning*, vol. 3, no. 1, pp. 1–122, 2011.
- [13] J. Fang, Z. Xu, B. Zhang, W. Hong, and Y. Wu, "Fast compressed sensing sar imaging based on approximated observation," *IEEE Journal of Selected Topics in Applied Earth Observations and Remote Sensing*, vol. 7, no. 1, pp. 352–363, 2013.
- [14] R. Baraniuk and P. Steeghs, "Compressive radar imaging," in *2007 IEEE radar conference*, IEEE, 2007, pp. 128–133.
- [15] B. Zhang, W. Hong, and Y. Wu, "Sparse microwave imaging: Principles and applications," *Science China Information Sciences*, vol. 55, no. 8, pp. 1722–1754, 2012.
- [16] A. Ribes and F. Schmitt, "Linear inverse problems in imaging," *IEEE Signal Processing Magazine*, vol. 25, no. 4, pp. 84–99, 2008.
- [17] J. A. Tropp and A. C. Gilbert, "Signal recovery from random measurements via orthogonal matching pursuit," *IEEE Transactions on information theory*, vol. 53, no. 12, pp. 4655–4666, 2007.
- [18] D. Needell and J. A. Tropp, "Cosamp: Iterative signal recovery from incomplete and inaccurate samples," *Applied and computational harmonic analysis*, vol. 26, no. 3, pp. 301–321, 2009.
- [19] A. Beck and M. Teboulle, "A fast iterative shrinkage-thresholding algorithm for linear inverse problems," *SIAM journal on imaging sciences*, vol. 2, no. 1, pp. 183–202, 2009.
- [20] F. Shen, G. Zhao, Z. Liu, G. Shi, and J. Lin, "Sar imaging with structural sparse representation," *IEEE Journal of Selected Topics in Applied Earth Observations and Remote Sensing*, vol. 8, no. 8, pp. 3902–3910, 2014.
- [21] A. Soni and J. Haupt, "Learning sparse representations for adaptive compressive sensing," in *2012 IEEE International Conference on Acoustics, Speech and Signal Processing (ICASSP)*, IEEE, 2012, pp. 2097–2100.
- [22] S. Samadi, M. Çetin, and M. A. Masnadi-Shirazi, "Multiple feature-enhanced sar imaging using sparsity in combined dictionaries," *IEEE Geoscience and Remote Sensing Letters*, vol. 10, no. 4, pp. 821–825, 2012.
- [23] C. Jiang, B. Zhang, J. Fang, *et al.*, "Efficient l_q regularisation algorithm with range–azimuth decoupled for sar imaging," *Electronics Letters*, vol. 50, no. 3, pp. 204–205, 2014.
- [24] P. Wang, H. Zhang, and V. M. Patel, "Sar image despeckling using a convolutional neural network," *IEEE Signal Processing Letters*, vol. 24, no. 12, pp. 1763–1767, 2017.
- [25] X. Zhou, K. Yang, and R. Duan, "Deep learning based on striation images for underwater and surface target classification," *IEEE signal processing letters*, vol. 26, no. 9, pp. 1378–1382, 2019.
- [26] J. Gao, B. Deng, Y. Qin, H. Wang, and X. Li, "Enhanced radar imaging using a complex-valued convolutional neural network," *IEEE Geoscience and Remote Sensing Letters*, vol. 16, no. 1, pp. 35–39, 2018.
- [27] H. Mu, Y. Zhang, C. Ding, Y. Jiang, M. H. Er, and A. C. Kot, "Deepimaging: A ground moving target imaging based on cnn for sar-gmti system," *IEEE Geoscience and Remote Sensing Letters*, vol. 18, no. 1, pp. 117–121, 2020.
- [28] S. B. Shah, P. Pradhan, W. Pu, R. Randhi, M. R. Rodrigues, and Y. C. Eldar, "Optimization guarantees of unfolded ista and admm networks with smooth soft-thresholding," *IEEE Transactions on Signal Processing*, 2024.
- [29] S. Wei, J. Liang, M. Wang, J. Shi, X. Zhang, and J. Ran, "Af-ampnet: A deep learning approach for sparse aperture isar imaging and autofocusing," *IEEE Transactions on Geoscience and Remote Sensing*, vol. 60, pp. 1–14, 2021.
- [30] M. Wang, S. Wei, J. Liang, S. Liu, J. Shi, and X. Zhang, "Lightweight fista-inspired sparse reconstruction network for mmw 3-d holography," *IEEE Transactions on Geoscience and Remote Sensing*, vol. 60, pp. 1–20, 2021.
- [31] S. Chen, Y. C. Eldar, and L. Zhao, "Graph unrolling networks: Interpretable neural networks for graph signal denoising," *IEEE Transactions on Signal Processing*, vol. 69, pp. 3699–3713, 2021.
- [32] V. Kouni and Y. Panagakis, "Deconet: An unfolding network for analysis-based compressed sensing with generalization error bounds," *IEEE Transactions on Signal Processing*, vol. 71, pp. 1938–1951, 2023.
- [33] Y. Wu, R. Song, Z. Zhang, X. Qiu, and W. Yu, "Gsat-net: An azimuth ambiguity suppression network based on group sparsity and adaptive threshold for under-sampling sar imaging," *IEEE Geoscience and Remote Sensing Letters*, 2024.
- [34] Y. Wu, Z. Zhang, X. Qiu, Y. Zhao, and W. Yu, "Mf-jmodl-net: A sparse sar imaging network for undersampling pattern design towards suppressed azimuth ambiguity," *IEEE Transactions on Geoscience and Remote Sensing*, 2024.
- [35] M. Li, J. Wu, W. Huo, *et al.*, "Target-oriented sar imaging for scr improvement via deep mf-admm-net," *IEEE Transactions on Geoscience and Remote Sensing*, vol. 60, pp. 1–14, 2022.
- [36] H. An, R. Jiang, J. Wu, *et al.*, "Lrsr-admm-net: A joint low-rank and sparse recovery network for sar imaging," *IEEE Transactions on Geoscience and Remote Sensing*, vol. 60, pp. 1–14, 2022.
- [37] J. Wu, W. Pu, H. An, Y. Huang, H. Yang, and J. Yang, "Learning-based high-frame-rate sar imaging," *IEEE Transactions on Geoscience and Remote Sensing*, vol. 61, pp. 1–13, 2023.

- [38] H. Zhang, J. Ni, S. Xiong, Y. Luo, and Q. Zhang, "Sr-ista-net: Sparse representation-based deep learning approach for sar imaging," *IEEE Geoscience and Remote Sensing Letters*, vol. 19, pp. 1–5, 2022.
- [39] H. Zhang, J. Ni, K. Li, Y. Luo, and Q. Zhang, "Non-sparse sar scene imaging network based on sparse representation and approximate observations," *Remote Sensing*, vol. 15, no. 17, p. 4126, 2023.
- [40] J. Yang, H. Zuo, H. An, *et al.*, "Sar non-sparse scene reconstruction network via image feature representation learning," *IEEE Transactions on Geoscience and Remote Sensing*, 2024.
- [41] S. V. Venkatakrishnan, C. A. Bouman, and B. Wohlberg, "Plug-and-play priors for model based reconstruction," in *2013 IEEE global conference on signal and information processing*, IEEE, 2013, pp. 945–948.
- [42] Y. Yang, J. Sun, H. Li, and Z. Xu, "Admm-csnet: A deep learning approach for image compressive sensing," *IEEE transactions on pattern analysis and machine intelligence*, vol. 42, no. 3, pp. 521–538, 2018.
- [43] C. Space, *Sar 101: An introduction to synthetic aperture radar*, <https://www.capellaspace.com/blog/sar-101-an-introduction-to-synthetic-aperture-radar>, 2020.
- [44] X. Dong and Y. Zhang, "A novel compressive sensing algorithm for sar imaging," *IEEE Journal of selected topics in applied earth observations and remote sensing*, vol. 7, no. 2, pp. 708–720, 2013.
- [45] R. Tomioka and M. Sugiyama, "Dual-augmented lagrangian method for efficient sparse reconstruction," *IEEE Signal Processing Letters*, vol. 16, no. 12, pp. 1067–1070, 2009.
- [46] Y. Wang, Z. He, X. Zhan, Q. Zeng, and Y. Hu, "A 3-d sparse sar imaging method based on plug-and-play," *IEEE Transactions on Geoscience and Remote Sensing*, vol. 60, pp. 1–14, 2022.
- [47] A. van den Bos, "Complex gradient and hessian," *IEE Proceedings-Vision, Image and Signal Processing*, vol. 141, no. 6, pp. 380–382, 1994.
- [48] S. Ioffe and C. Szegedy, "Batch normalization: Accelerating deep network training by reducing internal covariate shift," in *International conference on machine learning*, pmlr, 2015, pp. 448–456.
- [49] A. F. Agarap, "Deep learning using rectified linear units (relu)," *arXiv preprint arXiv:1803.08375*, 2018.
- [50] K. He, X. Zhang, S. Ren, and J. Sun, "Deep residual learning for image recognition," in *Proceedings of the IEEE conference on computer vision and pattern recognition*, 2016, pp. 770–778.
- [51] N. Ketkar, J. Moolayil, N. Ketkar, and J. Moolayil, "Introduction to pytorch," *Deep learning with python: learn best practices of deep learning models with PyTorch*, pp. 27–91, 2021.
- [52] D. P. Kingma and J. Ba, "Adam: A method for stochastic optimization," *arXiv preprint arXiv:1412.6980*, 2014.
- [53] A. Moreira, "Suppressing the azimuth ambiguities in synthetic aperture radar images," *IEEE Transactions on Geoscience and Remote Sensing*, vol. 31, no. 4, pp. 885–895, 1993.
- [54] R. Baraniuk, M. Davenport, R. DeVore, and M. Wakin, "A simple proof of the restricted isometry property for random matrices," *Constructive approximation*, vol. 28, pp. 253–263, 2008.
- [55] J. Castorena and C. D. Creusere, "The restricted isometry property for banded random matrices," *IEEE Transactions on Signal Processing*, vol. 62, no. 19, pp. 5073–5084, 2014.
- [56] A. A. Poli and M. C. Cirillo, "On the use of the normalized mean square error in evaluating dispersion model performance," *Atmospheric Environment. Part A. General Topics*, vol. 27, no. 15, pp. 2427–2434, 1993.
- [57] A. Hore and D. Ziou, "Image quality metrics: Psnr vs. ssim," in *2010 20th international conference on pattern recognition*, IEEE, 2010, pp. 2366–2369.
- [58] N. Tsagkarakis, P. P. Markopoulos, G. Sklivanitis, and D. A. Pados, "L1-norm principal-component analysis of complex data," *IEEE Transactions on Signal Processing*, vol. 66, no. 12, pp. 3256–3267, 2018.
- [59] F. I. Karahanoglu, I. Bayram, and D. Van De Ville, "A signal processing approach to generalized 1-d total variation," *IEEE Transactions on Signal Processing*, vol. 59, no. 11, pp. 5265–5274, 2011.
- [60] P. Duhamel and M. Vetterli, "Fast fourier transforms: A tutorial review and a state of the art," *Signal processing*, vol. 19, no. 4, pp. 259–299, 1990.